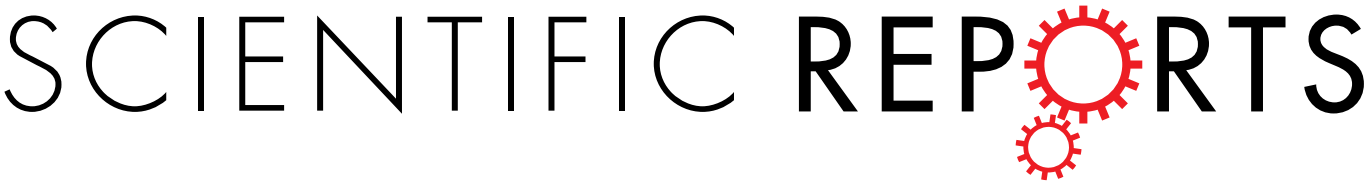

OPEN

Few-layer bismuth selenides exfoliated by hemin inhibit amyloid-β_{1-42} fibril formation

Received: 18 June 2014
Accepted: 01 April 2015
Published: 28 May 2015

Jian Peng[1,2], Yunjing Xiong[2], Zhiqin Lin[2], Liping Sun[2] & Jian Weng[2,3]

Inhibiting amyloid-β (Aβ) fibril formation is the primary therapeutic strategy for Alzheimer's disease. Several small molecules and nanomaterials have been used to inhibit Aβ fibril formation. However, insufficient inhibition efficiency or poor metabolization limits their further applications. Here, we used hemin to exfoliate few-layer Bi_2Se_3 in aqueous solution. Then we separated few-layer Bi_2Se_3 with different sizes and thicknesses by fractional centrifugation, and used them to attempt to inhibit $A\beta_{1-42}$ aggregation. The results show that smaller and thinner few-layer Bi_2Se_3 had the highest inhibition efficiency. We further investigated the interaction between few-layer Bi_2Se_3 and $A\beta_{1-42}$ monomers. The results indicate that the inhibition effect may be due to the high adsorption capacity of few-layer Bi_2Se_3 for $A\beta_{1-42}$ monomers. Few-layer Bi_2Se_3 also decreased Aβ-mediated peroxidase-like activity and cytotoxicity according to *in vitro* neurotoxicity studies under physiological conditions. Therefore, our work shows the potential for applications of few-layer Bi_2Se_3 in the biomedical field.

Alzheimer's disease (AD), one of the leading causes of death in the world[1], is a devastating neurodegenerative disorder and the most common form of dementia among people over the age of sixty-five. Senile plaques formed by the aggregation of Aβ peptides and neurofibrillary tangles comprised of primarily hyperphosphorylated tau in the brain are considered the pathologic hallmarks in AD[2]. According to the "Aβ hypothesis", Aβ is generated from specific β- and γ-secretase cleavages of amyloid precursor protein[3,4]. Aβ-protein (1–40) ($A\beta_{1-40}$) and Aβ-protein (1–42) ($A\beta_{1-42}$), which only differ in the two extra C-terminal residues, are the main component of extracellular senile plaques. Though $A\beta_{1-40}$ is 10 times more abundant than $A\beta_{1-42}$, $A\beta_{1-42}$ aggregates faster and plays an important role in AD development[5,6]. $A\beta_{1-42}$ with a molecular weight of 4.5 kDa is an amphipathic polypeptide, which is prone to aggregate and form fibrils[7]. It is reported that the aggregation and deposition of $A\beta_{1-42}$ in the brain is implicated in the aetiology of AD[8], and inhibiting Aβ aggregation has been thought as one of the primary therapeutic strategies for AD[9,10]. Therefore, screening Aβ inhibitors is very important in the research of AD. However, it remains a challenge to find an effective inhibitor for Aβ aggregation.

There are several publications that suggest some small molecules might serve as Aβ inhibitors to prevent amyloid fibril formation. Potential inhibitors with different structures have been reported, such as peptide fragments[11], organic dyes[12] and small aromatic compounds[13-15]. However, there are several challenges for small molecules to inhibit Aβ aggregation[16]. First, the interactions between protein and small molecule may be weak[17], resulting in insufficient efficiency to inhibit Aβ aggregation[18]. Second, small molecules may be accommodated by the highly plastic nature of protein surfaces, thus decreasing inhibition efficiency[19]. To solve these problems, new Aβ inhibitors are in urgent demand. Interestingly, nanomaterials have been used to inhibit Aβ fibril formation. Among them gold nanoparticles (NPs)[9,20], magnetic NPs[21], quantum dots[22], polymeric NPs[23], graphene oxide[24], carbon nanotubes[25] and polyoxometalate with

[1]College of Chemistry and Chemical Engineering, Xiamen University, Xiamen 361005, P.R. China. [2]College of Materials, Xiamen University, Xiamen 361005, P.R. China. [3]ShenZhen Research Institute of Xiamen University, Shenzhen 518057, China. Correspondence and requests for materials should be addressed to L.S. (email: sunliping@xmu.edu.cn) or J.W. (email: jweng@xmu.edu.cn)

a Wells–Dawson structure[26] have been used to inhibit Aβ fibril formation. However, there are also several challenges for nanomaterials to serve as Aβ inhibitors. The first problem is that these nanomaterials cannot be degraded, and are poorly metabolized. The second problem is that most of them fail to reduce Aβ-mediated neurotoxicity and peroxidase-like activity[27,28]. Furthermore, their inhibition mechanism has not been fully understood. To solve these problems, it is important to find new biocompatible materials that could be used to effectively inhibit Aβ aggregation.

Bismuth selenide (Bi_2Se_3), a topological insulator, has attracted wide interest in condensed matter physics due to the unique surface electronic states[29-31]. It consists of stacked layers of a laminated structure held together by weak van der Waals interactions. The three-dimensional (3D) structure restricts its application due to the bulk state of high carrier density[32]. Thus, the production of two-dimensional (2D) Bi_2Se_3 from its 3D bulk materials is in urgent demand in order to acquire superior property for potential applications. Up to now, 2D nanomaterials were mainly prepared by bottom-up synthesis and top-down exfoliation[33]. 3D materials with weak van der Waals forces can be exfoliated into thin flakes by mechanical or chemical exfoliation[34,35], which is a top-down process. This method has been used to produce single-layer or few-layer 2D materials such as graphene and few-layer molybdenum sulfide because it is easier and more convenient than other methods[36,37]. Therefore, we try to prepare few-layer Bi_2Se_3 by exfoliation of bulk Bi_2Se_3 in solution. Though 2D few-layer Bi_2Se_3 shows excellent properties which can be compared with graphene, there are only a few publications on the biomedical applications of Bi_2Se_3[38-41]. At the same time, the Se element can inhibit reactive oxygen species[42]. The Bi element, with atomic number 83, has a high photoelectric absorption coefficient and may be used as a cancer radio-sensitizer and X-ray contrast agent. Therefore, Bi_2Se_3 has been reported to serve as a theranostic reagent for simultaneous cancer imaging and therapy[40]. More importantly, it has been reported that Bi_2Se_3 nanoplates show low toxicity for mice even at high doses of 20 mg kg^{-1}. More surprisingly, Bi_2Se_3 nanoplates can be metabolized after long-term toxicological responses[41]. These properties of 2D Bi_2Se_3 stimulated us to investigate the interaction of 2D Bi_2Se_3 and Aβ, and explore its ability to inhibit Aβ fibril formation.

In order to combine the two advantages of 2D nanomaterials and small molecules in inhibiting Aβ fibril formation, we prepared few-layer Bi_2Se_3 coated by small molecules and investigated its ability to inhibit Aβ fibril formation. Here, few-layer Bi_2Se_3 exfoliated by hemin (Supplementary Fig. S1) was used to inhibit Aβ fibril formation under near-physiological conditions *in vitro* with satisfactory results. The preparation and application of exfoliated few-layer Bi_2Se_3 are simple, low cost and environmental-friendly. These advantages indicate that our present work could provide new insights into the potential application of 2D few-layer Bi_2Se_3 in medicine and biotechnology.

Results

Preparation and characterization of bulk Bi_2Se_3. Bulk Bi_2Se_3 was prepared by hydrothermal synthesis. The as-synthesized bulk Bi_2Se_3 exhibits sheet-like structure with a wide size distribution and is inclined to aggregate together, which was confirmed by scanning electron microscopy (SEM) and transmission electron microscopy (TEM) (Supplementary Fig. S2a, b). The selected area electron diffraction (SAED) pattern (Supplementary Fig. S2c) showed that Bi_2Se_3 was indexed as a 6-fold symmetry [001] zone axis pattern, which is consistent with the layered structure along the z axis. Then, energy dispersive X-ray (EDX) spectrum was employed to confirm the elementary composition of Bi_2Se_3 (Supplementary Fig. S2d). Furthermore, the thickness of bulk Bi_2Se_3 was about 50 nm, as-determined by atomic force microscopy (AFM, Supplementary Fig. S2e). Finally, the as-synthesized bulk Bi_2Se_3 was investigated by X-ray diffraction (XRD, Fig. 1f). All the labeled peaks were readily indexed as rhombohedral Bi_2Se_3 (JCPDS no. 89-2008).

Optimization of exfoliation conditions. The as-prepared bulk Bi_2Se_3 was firstly dispersed in hemin dissolved in 0.1% ammonia water ($NH_3{\cdot}H_2O$) solution. Then the mixture was sonicated for about 40 h to form few-layer Bi_2Se_3. Hemin, an iron-containing porphyrin small molecule, plays an important role in dispersing few-layer Bi_2Se_3. Therefore, it was necessary to investigate the effect of hemin concentration on the yield of few-layer Bi_2Se_3 (Supplementary Fig. S3). The results showed that the optimal concentration of hemin was 0.05 mg mL^{-1}. $NH_3{\cdot}H_2O$ solution also plays an important role in dissolving hemin, which can affect the yield of few-layer Bi_2Se_3 (Supplementary Fig. S4a, b). 0.1% is the optimal concentration of $NH_3{\cdot}H_2O$. We further explored the effect of pH on the yield of few-layer Bi_2Se_3 (Supplementary Fig. S4c, d). The pH was adjusted by 0.1 M sodium hydroxide (NaOH) solution to substitute $NH_3{\cdot}H_2O$ and 10 was the optimal pH that was close to the pH of 0.1% $NH_3{\cdot}H_2O$. We owe the exfoliation of bulk Bi_2Se_3 materials to the energy provided by the ultrasound waves, which overcome the van der Waals forces between Bi_2Se_3 layers. Therefore, the ultrasonic time is also an important parameter that should be investigated (Supplementary Fig. S5). The yield of few-layer Bi_2Se_3 was improved with increasing ultrasonic time; however, above an ultrasonic time of 40 h there was little change in the yield of few-layer Bi_2Se_3, and as such 40 h was chosen as the optimal ultrasonic time.

Characterization of few-layer Bi_2Se_3. Ultraviolet-visible (UV-vis) absorption spectra of the mixture of hemin and Bi_2Se_3 before and after sonication were measured, respectively (Supplementary Fig. S6a). Before sonication, the solution exhibited a brown color and the spectrum of the mixture had a strong peak at 388 nm attributed to the Soret band of hemin, as well as a group of weak peaks between

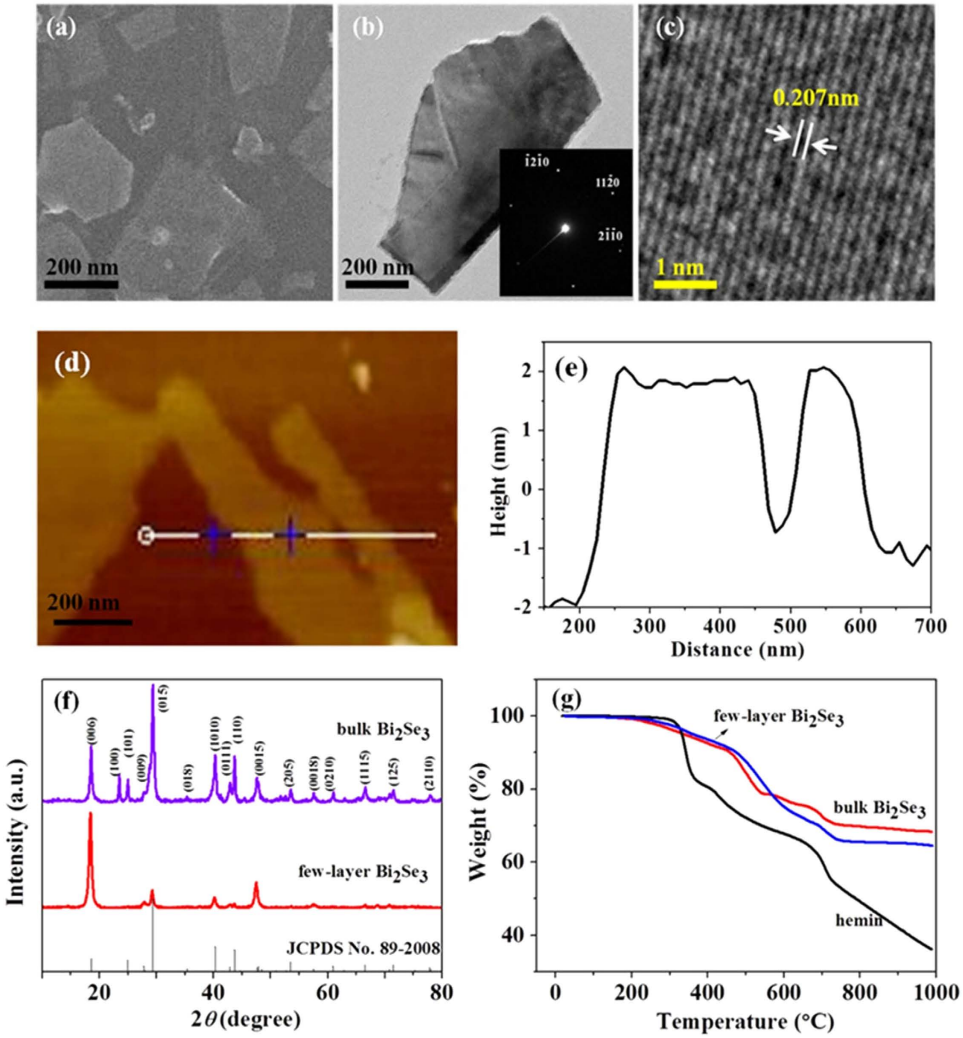

Figure 1. Few-layer Bi_2Se_3 exfoliated with hemin (0.05 mg mL^{-1}) in 0.1% $NH_3 \cdot H_2O$. (a) SEM image of few-layer Bi_2Se_3. (b) TEM image of few-layer Bi_2Se_3, insert: SAED pattern of few-layer Bi_2Se_3. (c) HRTEM image of few-layer Bi_2Se_3. (d, e) AFM image and the corresponding height profile of few-layer Bi_2Se_3. (f) XRD patterns of bulk and few-layer Bi_2Se_3. (g) TGA curves for hemin, bulk Bi_2Se_3 and few-layer Bi_2Se_3 in N_2 atmosphere with a ramp of 10°C min^{-1}.

500 and 700 nm ascribed to the Q-bands of hemin[43]. After sonication of 40 h, the color of solution changed from brown to gray (Supplementary Fig. S6b), maximum absorption band of the Soret band of hemin was red-shifted from 388 to 403 nm and a broad absorption in the visible light region appeared. These results are similar to few-layer Bi_2Se_3 exfoliated by N-methyl-2-pyrrolidone in our previous work[44], which could be attributed to the formation of few-layer Bi_2Se_3. At the same time, the absorption also increased gradually as the sonication time was extended (Supplementary Fig. S5), which revealed that more few-layer Bi_2Se_3 could be obtained with increasing sonication time. This suggests that the absorption was as a result of few-layer Bi_2Se_3.

The as-obtained few-layer Bi_2Se_3 was a thin 2D flake according to the SEM (Fig. 1a) and TEM images (Fig. 1b). Furthermore, according to the SAED pattern (Fig. 1b insert), few-layer Bi_2Se_3 was indexed as a 6-fold symmetry [001] zone axis pattern, which is consistent with the layered structure along the z axis. Also, it revealed the single-crystalline nature of the thin 2D flake. The distance between the adjacently hexagonal lattice fringes investigated by the HRTEM was 0.207 nm for Bi_2Se_3 (Fig. 1c), which is consistent with the lattice space of the (110) plane. The AFM image (Fig. 1d) also showed the flake structure and the thickness of exfoliated Bi_2Se_3 was 3-4 nm (Fig. 1e), which nearly equals to 3-4 layers of Bi_2Se_3[45]. The XRD pattern (Fig. 1f) of few-layer Bi_2Se_3 showed a high degree of [001] orientation and some characteristic peaks disappeared compared to bulk Bi_2Se_3, which indicated that bulk Bi_2Se_3 had been successfully exfoliated. To further confirm the exfoliation of Bi_2Se_3, Raman spectrum was employed (Supplementary Fig. S7). The A^1_{1g} mode of few-layer Bi_2Se_3 produced a red shift compared with that of bulk Bi_2Se_3, which

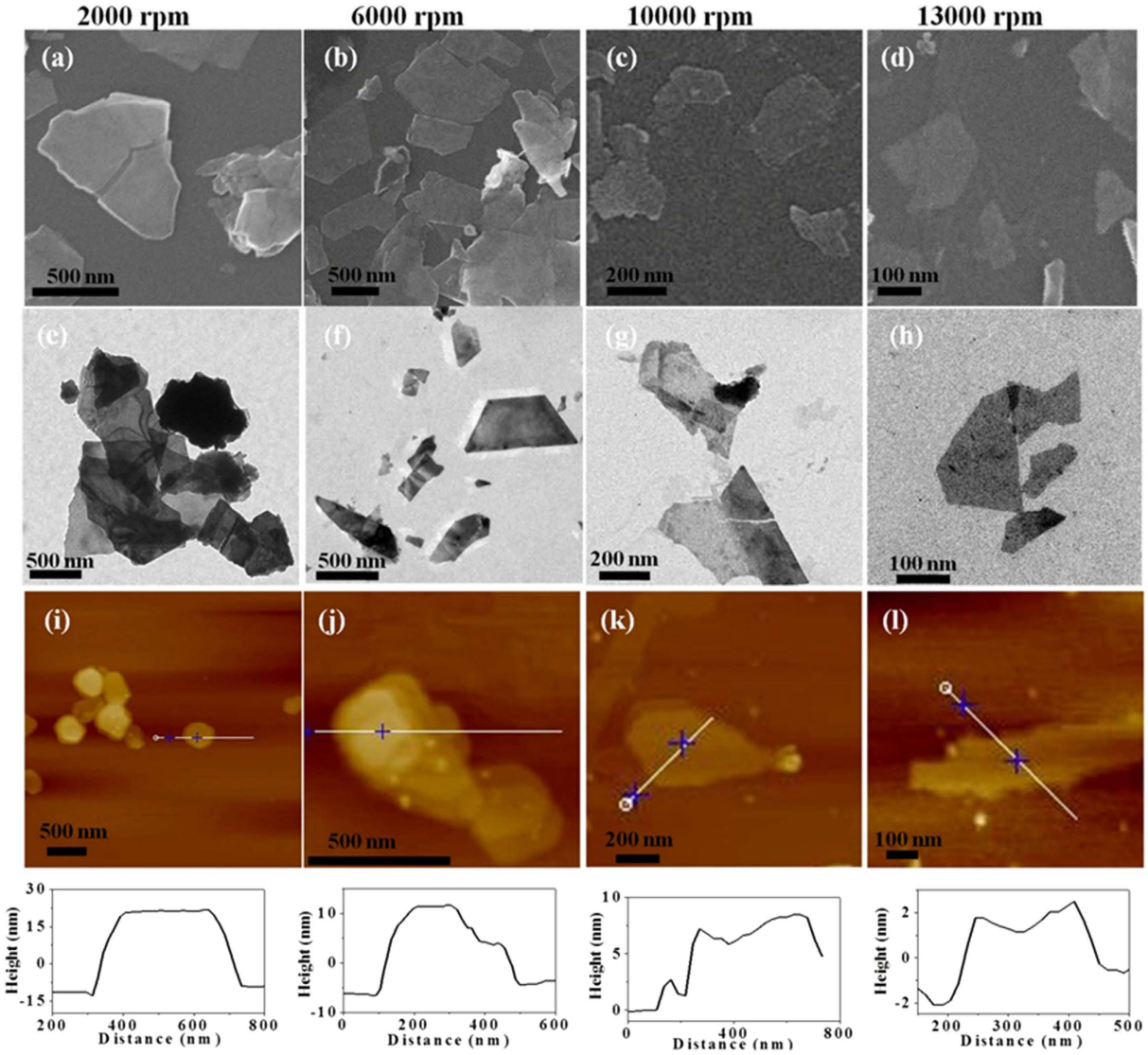

Figure 2. Few-layer Bi_2Se_3 with different layers. SEM, TEM and AFM images of few-layer Bi_2Se_3 stock solutions handled at 2000 (a, e, i), 6000 (b, f, j), 10000 (c, g, k) and 13000 rpm (d, h, l), respectively.

could be attributed to the phonon softening[46]. Furthermore, the content of hemin in few-layer Bi_2Se_3 was 11.8%, as calculated by thermogravimetric (TGA) analysis (Fig. 1g), which is consistent with the calculated value (12.0%) by X-ray photoelectron spectroscopy (XPS) and EDX (Supplementary Fig. S8).

Preparation of few-layer Bi_2Se_3 with different thicknesses. Fractional centrifugation was employed here to obtain few-layer Bi_2Se_3 with different layers. Firstly, the few-layer Bi_2Se_3 was characterized by UV-vis absorption spectra (Supplementary Fig. S9). Interestingly, we found that the dispersion solutions of few-layer Bi_2Se_3 produced a broad absorption in the visible light region compared to bulk Bi_2Se_3. Furthermore, few-layer Bi_2Se_3 stock solutions handled at different centrifugal speeds demonstrated different UV-vis absorption spectra. With centrifugal speed increasing from 2000 to 13000 rpm, the maximum absorption band of sample was blue-shifted gradually from 570 to 400 nm, resulting from quantum size effect[44], which indicated the production of few-layer Bi_2Se_3 with different sizes and layers.

The size distribution and corresponding height profile of few-layer Bi_2Se_3 collected at different centrifugation speeds were distinctive. TEM and SEM were used to measure the sizes of few-layer Bi_2Se_3 (Fig. 2). With centrifugal speed increasing from 2000 to 13000 rpm, the size of sample decreased gradually from 637 ± 183 to 105 ± 31 nm, indicating the production of few-layer Bi_2Se_3 with different sizes (Table 1). AFM is frequently used to character 2D materials. Here we used it to investigate the thickness of few-layer Bi_2Se_3. With centrifugal speed increasing from 2000 to 13000 rpm, the thickness of few-layer Bi_2Se_3 decreased from about 40 to 3 nm (Fig 2.i-l), which further indicated the production of few-layer Bi_2Se_3 with different layers.

Inhibitor	Hemin	Mixture	2000 rpm	6000 rpm	10000 rpm	13000 rpm
Size (nm) [a]	/	447 ± 373	637 ± 183	343 ± 73	243 ± 53	105 ± 31
Thickness (nm) [b]	/	10 ± 8	40 ± 10	15 ± 3	6 ± 2	3 ± 1
Inhibition efficiency (%) [c]	19.7	44.7	/[d]	33.7	51.7	67.4

Table 1. Size, thickness of few-layer Bi_2Se_3 at differently centrifugal speeds and their inhibition efficiency towards Aβ. (a) The size was obtained from TEM images. Mean and standard deviation are given, n = 10. (b) The thickness was obtained from AFM images. Mean and standard deviation are given, n = 10. (c) The inhibition efficiency was analyzed by ThT fluorescence assay. It is calculated as follows: Inhibition efficiency = $(F_0\text{-}F_i)/F_0 \times 100\%$, F_i and F_0 represent the ThT fluorescence intensity of $A\beta_{1\text{-}42}$ with and without inhibitor, respectively. $A\beta_{1\text{-}42}$ and inhibitor were incubated at 37°C for 3 h as showed in Fig.3. (d) Few-layer Bi_2Se_3 handled at 2000 rpm was thought as bulk Bi_2Se_3 which has not been exfoliated as expected. The dispersity of bulk Bi_2Se_3 in aqueous solution is poor.

Inhibiting $A\beta_{1\text{-}42}$ fibril formation by few-layer Bi_2Se_3. Thioflavine T (ThT) is a classic amyloid dye that is frequently used to probe Aβ fibril formation due to its strong fluorescence emission upon binding to cross-β fibril structures[47-49]. We co-incubated $A\beta_{1\text{-}42}$ monomer and few-layer Bi_2Se_3 with different concentrations, and then monitored Aβ fibril formation kinetics by ThT fluorescence assay. Modified Krebs-Henseliet buffer, which mimics near-physiological conditions[8], was used in the following experiments except where specifically noted. $A\beta_{1\text{-}42}$ fibril formation in modified Krebs-Henseliet buffer without few-layer Bi_2Se_3 was firstly investigated by ThT fluorescence assay (Supplementary Fig. S10). In the absence of few-layer Bi_2Se_3, $A\beta_{1\text{-}42}$ formed ThT-positive β-sheets instantaneously and ThT fluorescence reached maximum intensity at 3 h and then decreased gradually. Therefore, 3 h was selected as the appropriate time to study the effect of few-layer Bi_2Se_3 on $A\beta_{1\text{-}42}$ fibril formation. The Aβ fibril formation kinetics in the absence and presence of few-layer Bi_2Se_3 with different thicknesses are shown in Fig. 3. Before fractional centrifugation, few-layer Bi_2Se_3 with a wide thickness distribution (10 ± 8 nm) was named a mixture. When the mixture was introduced (Fig. 3a), the fluorescence intensity at 3 h gradually decreased with increasing concentration of few-layer Bi_2Se_3, indicating consistent inhibition of $A\beta_{1\text{-}42}$ fibril formation by few-layer Bi_2Se_3 in a dose-dependent manner. To further investigate the effect of few-layer Bi_2Se_3 thickness on $A\beta_{1\text{-}42}$ fibril formation, few-layer Bi_2Se_3 with different thicknesses were introduced (Fig. 3b-d). Similarly, fluorescence intensities at 3 h gradually decreased with increasing concentration of few-layer Bi_2Se_3. It is interesting that the fluorescence intensity at 3 h gradually decreased with decreasing thickness of few-layer Bi_2Se_3 at a same concentration, indicating the inhibition efficiency increased with decreasing layers of few-layer Bi_2Se_3 (Table 1 and Fig. 3f). Few-layer Bi_2Se_3 contains 11.8% hemin calculated by TGA and XPS data (Supplementary Fig. S8). In order to investigate the effect of hemin on $A\beta_{1\text{-}42}$ fibril formation, the corresponding hemin in few-layer Bi_2Se_3 with different concentrations was calculated and incubated with $A\beta_{1\text{-}42}$ monomer in similar conditions (Fig. 3e and Table 1). Compared with few-layer Bi_2Se_3, the decrease of ThT fluorescence intensity induced by hemin was negligible. Therefore, the high inhibition efficiency of few-layer Bi_2Se_3 resulted mainly from few-layer Bi_2Se_3 (Fig. 3f, Table 1). Finally, the end-point ThT intensities at 3 h versus different Aβ inhibitors were plotted (Fig. 3f) and few-layer Bi_2Se_3 of 3 ± 1 nm had the best efficiency in inhibiting Aβ fibril formation. Therefore, few-layer Bi_2Se_3 of 3 ± 1 nm was used in following experiments except where specifically noted.

To confirm that the reduced ThT fluorescence intensity resulted from the inhibiting $A\beta_{1\text{-}42}$ fibril formation by few-layer Bi_2Se_3, but not quenched by few-layer Bi_2Se_3 and hemin themselves, we investigated the effect of few-layer Bi_2Se_3 and hemin on ThT fluorescence intensity without $A\beta_{1\text{-}42}$ monomer (Supplementary Fig. S11). The change of ThT intensity after incubation with few-layer Bi_2Se_3 and hemin is unobvious. At the same time, the intrinsic fluorescence of hemin can also be neglected compared to ThT fluorescence of $A\beta_{1\text{-}42}$ fibril when the excitation wavelength is 442 nm (Supplementary Fig. S12). The results further suggest that the reduced ThT fluorescence intensity resulted from the inhibition of $A\beta_{1\text{-}42}$ fibril formation by few-layer Bi_2Se_3.

To further confirm the results of the ThT fluorescence assay, TEM and AFM were used to observe the morphologies of end-point products at 3 h (Fig. 4). After incubation of $A\beta_{1\text{-}42}$ monomer without few-layer Bi_2Se_3 at 37°C for 3 h, $A\beta_{1\text{-}42}$ formed long, smooth, and entangled fibrils as expected (Fig. 4a, g). However, after incubation of $A\beta_{1\text{-}42}$ monomer and few-layer Bi_2Se_3 with different concentrations, different Aβ species were observed. In the presence of 12 ng mL^{-1} few-layer Bi_2Se_3 (Fig. 4b), fewer negatively-stained fibrils were observed and generally shorter in length than that without few-layer Bi_2Se_3. $A\beta_{1\text{-}42}$ in the presence of 60 ng mL^{-1} few-layer Bi_2Se_3 formed some negatively-stained fibrils with amorphous aggregates (Fig. 4c, h) which were generally smaller in size than that without few-layer Bi_2Se_3. In the presence of 300 ng mL^{-1} few-layer Bi_2Se_3, primarily positively-stained aggregates with a small size were formed (Fig. 4d). However, $A\beta_{1\text{-}42}$ in the presence of 1200 ng mL^{-1} few-layer Bi_2Se_3 formed small

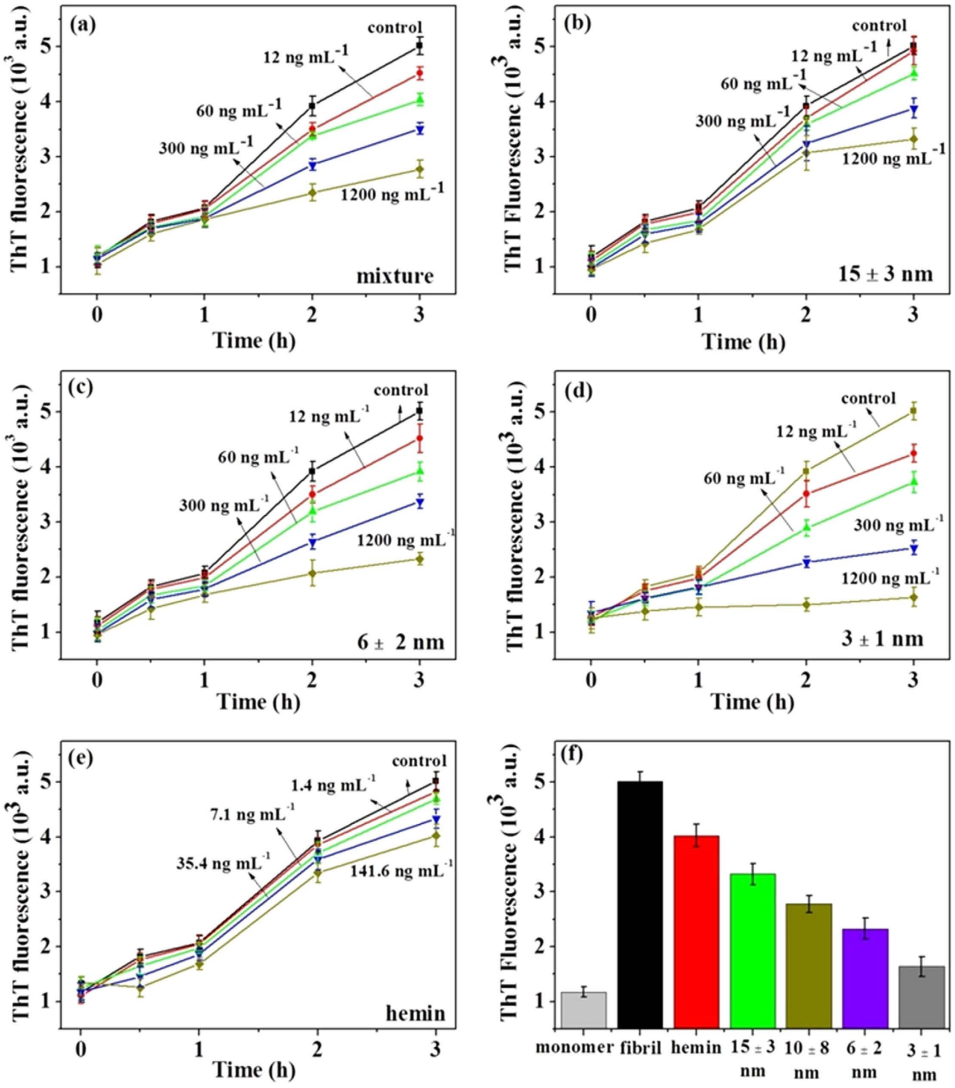

Figure 3. Inhibiting $A\beta_{1\text{-}42}$ fibril formation by few-layer Bi_2Se_3 with different thicknesses investigating by ThT assay. Kinetics of $A\beta_{1\text{-}42}$ fibril formation at 37°C in presence of few-layer Bi_2Se_3 with thickness of 10 ± 8 nm (mixture, a) , 15 ± 3 nm (b), 6 ± 2 nm (c), 3 ± 1 nm (d) and hemin (e). (f) ThT fluorescence intensity of $A\beta_{1\text{-}42}$ monomer, $A\beta_{1\text{-}42}$ fibril, $A\beta_{1\text{-}42}$ incubated at 37°C for 3 h in presence of hemin and few-layer Bi_2Se_3 with different thicknesses, respectively. Fluorescence emissions were monitored at 485 nm with excitation at 442 nm. Three replicates were performed.

particles adsorbed on few-layer Bi_2Se_3 and no fibrils were observed (Fig. 4e, f, i). The SAED pattern (Fig. 4f insert) indicated that the thin sheet was few-layer Bi_2Se_3. The AFM height profiles show that the size of $A\beta_{1\text{-}42}$ species decreased with increasing few-layer Bi_2Se_3 concentration, which further demonstrates that few-layer Bi_2Se_3 inhibits $A\beta_{1\text{-}42}$ fibril formation in a dose-dependent manner. The AFM height profile of $A\beta_{1\text{-}42}$ in the presence of 60 ng mL^{-1} few-layer Bi_2Se_3 was higher than that of $A\beta_{1\text{-}42}$ without few-layer Bi_2Se_3, which could be attributed to adsorption of $A\beta_{1\text{-}42}$ aggregates on few-layer Bi_2Se_3 surface. However, the AFM height profile of $A\beta_{1\text{-}42}$ in the presence of 1200 ng mL^{-1} few-layer Bi_2Se_3 is close to that of bare few-layer Bi_2Se_3, which could be attributed to adsorption of $A\beta_{1\text{-}42}$ monomers on few-layer Bi_2Se_3. TEM images of end-point products of $A\beta_{1\text{-}42}$ at 3 h in the presence of few-layer Bi_2Se_3 mixture with a thickness 10 ± 8 nm also demonstrated inhibition of $A\beta_{1\text{-}42}$ fibril formation by few-layer Bi_2Se_3 (Supplementary Fig. S13).

We employed dynamic light scattering (DLS) to study the size distribution of particles because DLS can provide a qualitative estimation of the aggregated state of $A\beta_{1\text{-}42}$ fibrils (Fig. 5). The freshly prepared $A\beta_{1\text{-}42}$ monomer in modified Krebs-Henseliet buffer has a hydrodynamic diameter around 4 nm (Fig. 5a). After incubation of $A\beta_{1\text{-}42}$ monomer without few-layer Bi_2Se_3 at 37°C for 3 h, large particles with a diameter about 1000 nm were observed. When 12 ng mL^{-1} few-layer Bi_2Se_3 was added, the peak at 1000 nm disappeared and broad peaks (400 nm – 4 μm) appeared, indicating parts of the $A\beta_{1\text{-}42}$ fibrils

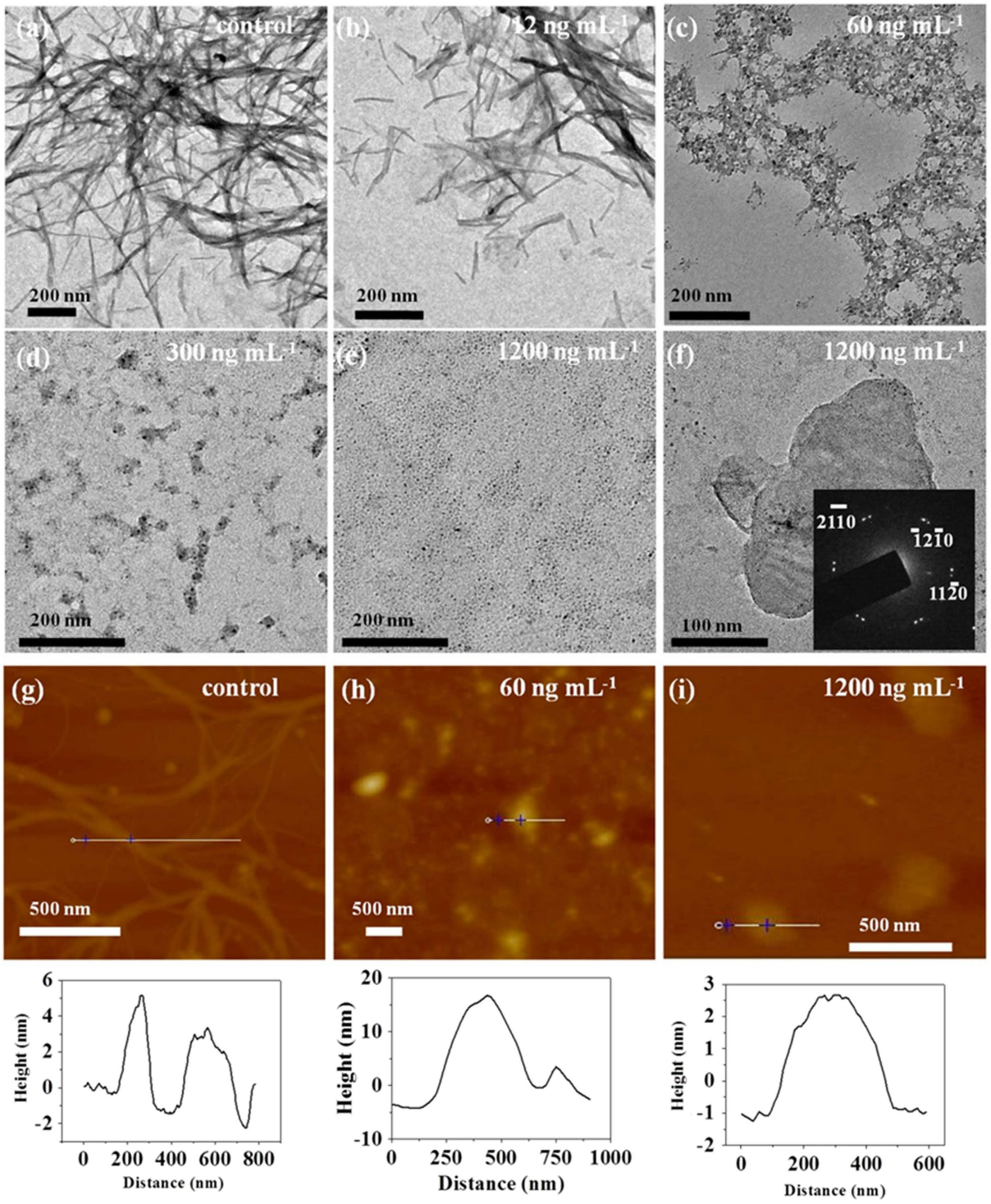

Figure 4. Few-layer Bi_2Se_3 inhibits $A\beta_{1-42}$ fibril formation monitored by TEM and AFM. Morphologies of the $A\beta_{1-42}$ species with and without few-layer Bi_2Se_3 (thickness, 3 ± 1 nm) with different concentrations monitored by TEM (a-f) and AFM (g-i). Insert in (f): SAED pattern of few-layer Bi_2Se_3. Corresponding height profiles of AFM were given below AFM. The concentration of few-layer Bi_2Se_3 and the scale bars were indicated in each image.

remained intact (Fig. 5c). At high concentration of few-layer Bi_2Se_3 (1200 ng mL^{-1}), no peak at 1000 nm was observed, indicating disappearance of large fibrils (Fig. 5d). The peak is almost the same as that of bare few-layer Bi_2Se_3 (Fig. 5e). These results further indicate that few-layer Bi_2Se_3 can inhibit $A\beta_{1-42}$ fibril formation.

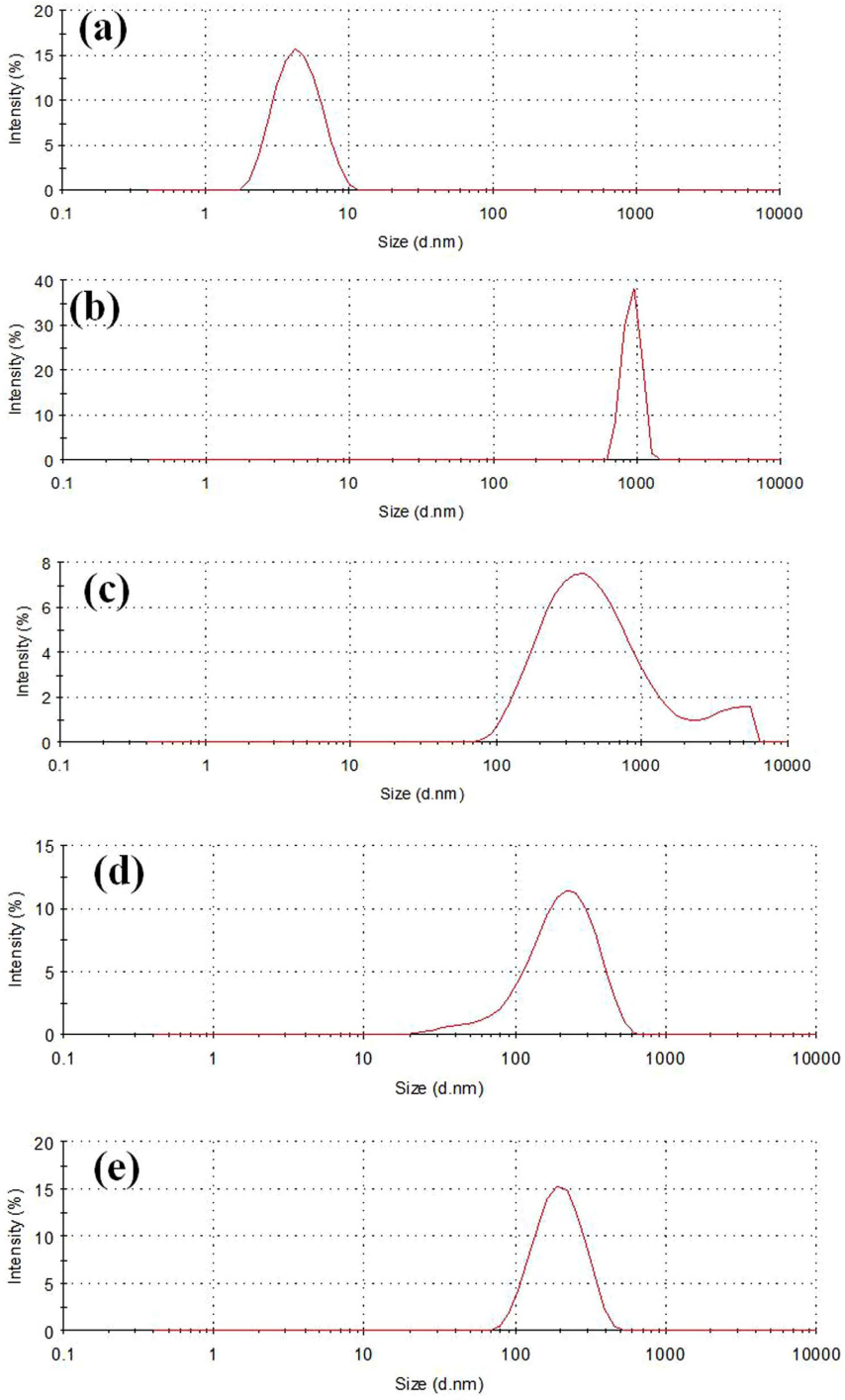

Figure 5. DLS analysis of inhibiting $A\beta_{1-42}$ fibril formation by few-layer Bi_2Se_3. (a) Freshly prepared $A\beta_{1-42}$ monomer. (b) $A\beta_{1-42}$ fibril after incubation of $A\beta_{1-42}$ monomer at 37°C for 3 h. (c) $A\beta_{1-42}$ with 12 ng mL^{-1} few-layer Bi_2Se_3 after incubation at 37°C for 3 h. (d) $A\beta_{1-42}$ with 1200 ng mL^{-1} few-layer Bi_2Se_3 after incubation at 37°C for 3 h. (d) Bare few-layer Bi_2Se_3.

Furthermore, polyacrylamide gel electrophoresis (PAGE) and cyclic voltammograms (CVs) were employed to confirm the inhibiting effect of few-layer Bi_2Se_3 on $A\beta_{1-42}$ fibril formation (Supplementary Fig. S14). $A\beta_{1-42}$ monomer, oligomer and fibril have different molecular weights. Freshly-prepared solution of $A\beta_{1-42}$ monomers displayed a strong band at 5 kDa, the molecular weight of $A\beta_{1-42}$ is 4.5 kDa. After incubation of $A\beta_{1-42}$ at 37°C for 3h, the monomer band (5 kDa) became weak and a band above 100 kDa appeared, indicating the formation of $A\beta_{1-42}$ fibrils. With the addition of few-layer Bi_2Se_3 from 12 to 1200 ng mL^{-1}, the fibril band became weaker and weaker. When 1200 ng mL^{-1} few-layer Bi_2Se_3 was added, the fibril band almost disappeared. To avoid the influence of SDS on $A\beta_{1-42}$ fibril formation, native

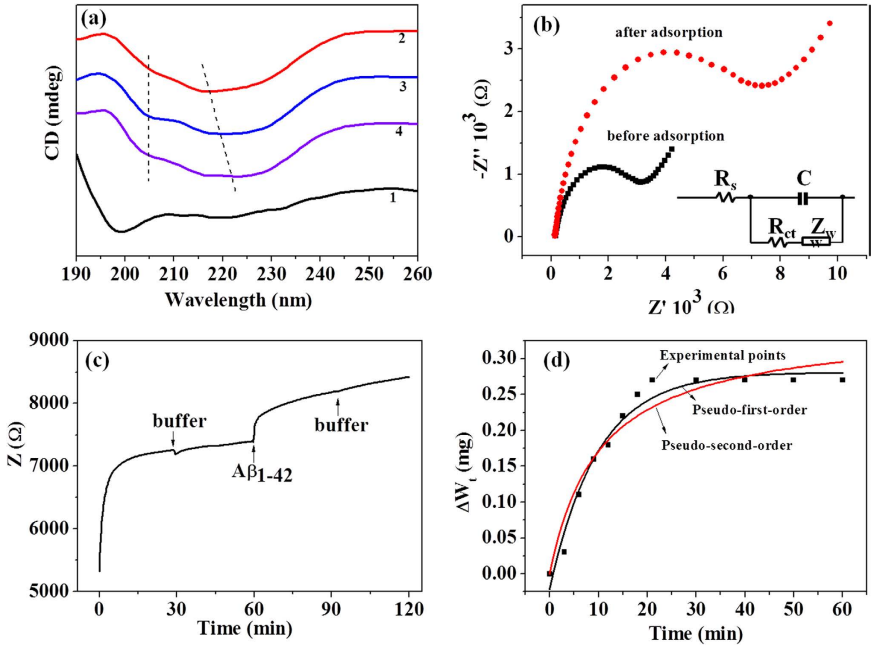

Figure 6. $A\beta_{1-42}$ monomer adsorbing on the surface of few-layer Bi_2Se_3. (a) CD spectra of $A\beta_{1-42}$ with and without few-layer Bi_2Se_3. (1): $A\beta_{1-42}$ monomer, (2-4): $A\beta_{1-42}$ was incubated at 37°C for 3 h in the presence of few-layer Bi_2Se_3 with different concentrations (2: 0, 3: 120 and 4: 2400 ng mL^{-1}, respectively). (b) Nyquist diagrams of few-layer Bi_2Se_3-modified GCE before and after adsorption of freshly prepared $A\beta_{1-42}$ monomer. Inset: equivalent circuit used to model impedance data in the presence of redox couples. R_s, electrolyte solution resistance; R_{ct}, interfacial electron transfer resistance; C, capacitance of the electric double layer between electrolyte and interface of electrode. The concentrations of few-layer Bi_2Se_3 and $A\beta_{1-42}$ monomer were 10 μg mL^{-1} and 10 μM, respectively. (c) Impedance at 10 Hz with time for few-layer Bi_2Se_3-modified GCE immersed in modified Krebs-Henseliet buffer. Buffer was added twice at 30 and 90 min, respectively. $A\beta_{1-42}$ monomer was added at 60 min. (d) Weight increment (ΔWt) with time was measured for few-layer Bi_2Se_3 coating silicon slice which was immersed in modified Krebs-Henseliet buffer containing 10 μM freshly-prepared $A\beta_{1-42}$ monomers.

PAGE was also performed (Supplementary Fig. S14c). After incubation for 3 h, native PAGE indicated that $A\beta_{1-42}$ in the absence of few-layer Bi_2Se_3 (lane 2) showed a decreased monomer band compared to freshly prepared $A\beta_{1-42}$ monomer (lane 1). However, when few-layer Bi_2Se_3 with different concentrations were added, the monomer band recovered in a dose-dependent manner. The relative quantity of monomer band was calculated from Supplementary Fig. S14c. These results show that few-layer Bi_2Se_3 can inhibit $A\beta_{1-42}$ fibril formation in a dose-dependent manner (Supplementary Fig. S14d).

The conductivities of $A\beta_{1-42}$ monomer and fibril on the electrode surface should be different. Therefore, we also investigated the conductivities of glassy carbon electrode (GCE) modified by few-layer Bi_2Se_3, $A\beta_{1-42}$ monomer and end-products of $A\beta_{1-42}$ at 3 h with and without few-layer Bi_2Se_3 (Supplementary Fig. S14b). GCE modified by few-layer Bi_2Se_3 showed good conductivity almost the same as GCE. In the presence of $A\beta_{1-42}$ monomer, there was a small decrease in conductivity. However, a large drop for conductivity was seen when $A\beta_{1-42}$ fibril was introduced, which can be attributed to the insulating property of the fibrils. Interestingly, the conductivity recovered when $A\beta_{1-42}$ with few-layer Bi_2Se_3 was introduced under the same concentration, further indicating that few-layer Bi_2Se_3 might effectively inhibit $A\beta_{1-42}$ fibril formation, which might be due to the adsorption of $A\beta_{1-42}$ monomers on few-layer Bi_2Se_3 to inhibit Aβ fibril formation.

Inhibition mechanism of $A\beta_{1-42}$ fibril formation by few-layer Bi_2Se_3. In order to investigate the inhibition mechanism, the inhibition process and the interaction of few-layer Bi_2Se_3 and $A\beta_{1-42}$ were investigated by circular dichroism (CD), XPS, microbalance, CVs and electrochemical impedance (Fig. 6). In order to investigate whether modification of the secondary structure of $A\beta_{1-42}$ monomer occurred in the presence of few-layer Bi_2Se_3, CD spectra were collected (Fig. 6a). Freshly-prepared $A\beta_{1-42}$ monomer displayed a negative peak below 200 nm corresponding to random-coil structure of the peptide. After incubation of $A\beta_{1-42}$ at 37°C for 3 h, $A\beta_{1-42}$ in the absence of few-layer Bi_2Se_3 displayed a negative peak at 217 nm corresponding to β-sheet structure of the peptide due to fibril formation. The peak was red-shifted to about 222 nm and a weak peak between 200 and 210 nm appeared with

	Pseudo-first-order model			Pseudo-second-order model		
$\Delta W_{0,exp}$ (mg)	$\Delta W_{0,cal}$ (mg)	k1 (min^{-1})	R^2	$\Delta W_{0,cal}$ (mg)	k2 (mg^{-1} min^{-1})	R^2
0.27	0.28	0.10	0.9698	0.35	0.28	0.9343

Table 2. Kinetic constants of the pseudo-first-order and pseudo-second-order kinetic models.

increasing concentration of few-layer Bi_2Se_3, which indicated the appearance of α-helix[50]. The percentage of different secondary structure for $A\beta_{1-42}$ monomer and $A\beta_{1-42}$ incubated at 37°C for 3 h in the presence and absence of few-layer Bi_2Se_3 was calculated by Jasco secondary structure estimation software (Supplementary Table. S1). These results indicate that few-layer Bi_2Se_3 may inhibit $A\beta_{1-42}$ fibril formation by preventing β-sheet structure formation.

In order to confirm that $A\beta_{1-42}$ monomer is adsorbed on the surface of few-layer Bi_2Se_3, CVs (Supplementary Fig. S15) and Nyquist diagrams (Fig. 6b) of few-layer Bi_2Se_3-modified GCE before and after adsorbing $A\beta_{1-42}$ monomer were collected. Before adsorption, few-layer Bi_2Se_3-modified GCE showed good conductivity and the electron transfer resistance (R_{ct}) is 2700 Ω. After adsorption, the conductivity decreased and the R_{ct} increased from 2700 to 7800 Ω, indicating that the $A\beta_{1-42}$ monomer had been successfully adsorbed on few-layer Bi_2Se_3. To further confirm the results, XPS and EDXA mapping images of few-layer Bi_2Se_3 before and after adsorbing $A\beta_{1-42}$ monomer were collected. XPS data demonstrated that the carbon, nitrogen and oxygen contents of few-layer Bi_2Se_3 after adsorbing $A\beta_{1-42}$ monomer increased from 48.87%, 5.9% and 21.72% to 54.90%, 10.3% and 30.25%, respectively (Supplementary Fig. S16), indicating adsorption of $A\beta_{1-42}$ monomer on the surface of few-layer Bi_2Se_3. EDXA mapping images showed that the $A\beta_{1-42}$ monomer was uniformly adsorbed on the surface of few-layer Bi_2Se_3 (Supplementary Fig. S17). These results motivated us to investigate the dynamics of the adsorbing process. First, few-layer Bi_2Se_3-modified GCE was prepared and immersed in modified Krebs-Henseliet buffer which buffer and $A\beta_{1-42}$ were added at different times, and impedance spectra with time was collected (Fig. 6c). No obvious impedance change was observed when the buffer was added at 30 and 90 min, while there was a large increase in impedance when $A\beta_{1-42}$ monomer was added at 60 min, which indicated that $A\beta_{1-42}$ monomer gradually adsorbed onto few-layer Bi_2Se_3. To quantify the adsorbing amount of $A\beta_{1-42}$ monomer, few-layer Bi_2Se_3-coated silicon wafer was hung on a microbalance and the weight was real-time monitored with $A\beta_{1-42}$ monomer adsorbed on the surface of few-layer Bi_2Se_3 (Fig. 6d). The weight increased gradually with time and reached equilibrium after 20 min. In order to examine the mechanism and rate-controlling step in the overall adsorption process, pseudo-first-order and pseudo-second-order kinetic models were used to investigate the adsorption process. The nonlinear forms are expressed as the following equations, respectively[51].

$$\Delta W_t = \Delta W_0 * (1 - \exp^{-k1t}) \quad (1)$$

$$\Delta W_t = k2 \Delta W_0^2 * t / (1 + k2 \Delta W_0 * t) \quad (2)$$

where ΔW_0 and ΔW_t are the adsorption amounts of $A\beta_{1-42}$ monomer at equilibrium and at time t, respectively. k1 and k2 are the rate constants of pseudo-first-order and pseudo-second-order kinetic equation, respectively.

Figure 6d shows the fitting curves by pseudo-first-order and pseudo-second-order kinetic equations. The fitting of pseudo-first-order kinetic curve overlaps with our experimental data and is better than that of pseudo-second-order kinetic curve. The kinetic parameters of two models are given in Table 2. The value of R^2 for equation (2) is 0.9343, and the calculated $\Delta W_{0,cal}$ is far from the experimental value of $\Delta W_{0,exp}$. The experimental value is consistent with the calculated value from pseudo-first-order kinetic fitting, suggesting the adsorption process can be well-described by the pseudo-first-order kinetic model. The zeta potentials of $A\beta_{1-42}$ monomer and few-layer Bi_2Se_3 are -16.3 and -29.4 mV, respectively (Supplementary Fig. S18). Therefore, it is unlikely that the adsorption of $A\beta_{1-42}$ monomer is due to electrostatic interactions. These results suggest that the adsorption rate is mainly controlled by hydrophobic interactions between hemin on the surface of few-layer Bi_2Se_3 and $A\beta_{1-42}$.

To represent the suggested mechanism, a simple schematic for $A\beta_{1-42}$ fibril formation with and without few-layer Bi_2Se_3 is depicted in Fig. 7. In the absence of few-layer Bi_2Se_3, $A\beta_{1-42}$ grows gradually into fibrils. In the 'nucleation phase', Aβ monomers with random-coil structure undergo conformational change and aggregate into oligomers. In the 'elongation phase', oligomers rapidly grow and form larger aggregates known as fibrils[52,53]. When few-layer Bi_2Se_3 with a low concentration (<300 ng mL^{-1}) is added, $A\beta_{1-42}$ monomers quickly adsorb on the surface of few-layer Bi_2Se_3 and grow to form some aggregates due to the relatively high concentration of $A\beta_{1-42}$, while free $A\beta_{1-42}$ monomers in solution aggregate into oligomers, then both $A\beta_{1-42}$ in solution and on few-layer Bi_2Se_3 aggregate into fibrils. However, when few-layer Bi_2Se_3 with a high concentration (>300 ng mL^{-1}) is added, most of $A\beta_{1-42}$ monomers quickly

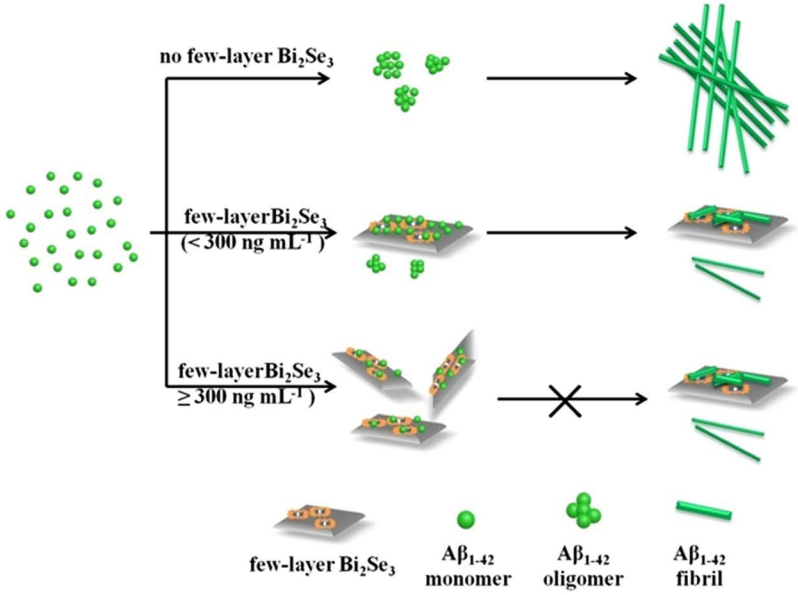

Figure 7. Inhibiting $A\beta_{1-42}$ fibril formation by few-layer Bi_2Se_3. Schematic of the mechanism by which few-layer Bi_2Se_3 may inhibit $A\beta_{1-42}$ fibril formation.

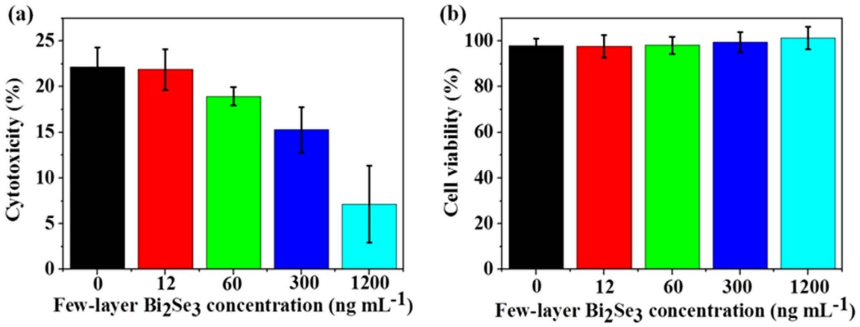

Figure 8. Few-layer Bi_2Se_3 reduces the cytoxicity induced by $A\beta_{1-42}$ fibrils for C6 rat glioma cells. Samples were prepared in the presence (a) or absence (b) of $A\beta_{1-42}$. The cytotoxic effect on C6 cells was determined by MTT assay from three separate measurements. Error bars indicate±s.d. Percentage of cytotoxicity was calculated as follows: Cytotoxicity = 100% - cell viability.

adsorb on the surface of few-layer Bi_2Se_3 uniformly. Thus, the amount of free $A\beta_{1-42}$ monomer in solution is low and cannot aggregate to form fibrils.

Reducing Aβ-mediated peroxidase-like activity and cytoxicity. Recently, heme has been reported to bind Aβ monomer, thus increasing peroxidase-like activity relative to free heme[28]. Therefore, we investigated the effect of few-layer Bi_2Se_3 on Aβ-mediated peroxidase-like activity (Supplementary Fig. S19). Hemin-Aβ complexes showed remarkably enhanced peroxidase-like activity relative to free hemin, which is consistent with a study[54]. However, when free hemin is replaced by few-layer Bi_2Se_3 containing the same amount of hemin, the enhanced peroxidase-like activity decreased to lower than that of free hemin, but a little higher than that of bare few-layer Bi_2Se_3. At the same time, few-layer Bi_2Se_3-Aβ complexes incubated at 37°C for 3 h also prevented enhanced peroxidase-like activity. Inhibition of enhanced peroxidase-like activity is attributed to the antioxidant effect of few-layer Bi_2Se_3. The results suggest that few-layer Bi_2Se_3 could serve as an effective inhibitor of Aβ-mediated peroxidase-like activity.

To assess the cytoxicity effect of few-layer Bi_2Se_3-induced $A\beta_{1-42}$ species, we performed 3-[4,5-Dimethylthiazol-2-yl]-2,5-diphenyltetrazdium bromide (MTT) assays to examine the activity of mitochondrial alcohol dehydrogenase by treating rat glioma cells, C6, with our end-point products at 3 h. Cytoxicity was demonstrated by the reduction of cell viability and the viability is normalized to the one treated with the buffer control. $A\beta_{1-42}$ fibril alone contributed to ~22% cytoxicity to the glioma cells (Fig. 8a). For the end-point products obtained from $A\beta_{1-42}$ monomer incubated with few-layer Bi_2Se_3 with different concentrations, the cytoxicity decreased with increasing concentration of few-layer Bi_2Se_3

in a dose-dependent manner. When few-layer Bi_2Se_3 concentration was 1200 ng mL^{-1}, the cytotoxicity was significantly reduced to ~7%. Furthermore, the toxicity of few-layer Bi_2Se_3 itself was evaluated by MTT assay (Fig. 8b). Few-layer Bi_2Se_3 itself with the concentration used above showed little cell toxicity under our experiment conditions. These results suggest that few-layer Bi_2Se_3 can inhibit $A\beta_{1-42}$-induced cell toxicity.

Discussion

In this paper, we successfully prepared few-layer Bi_2Se_3 by liquid-exfoliation with the aid of hemin and found that it could exhibit good performance in inhibiting Aβ fibril formation. There are three reasons that hemin is selected as a stabilizer to exfoliate bulk Bi_2Se_3. First, hemin, iron protoporphyrin, is the active center of heme-proteins, such as cytochromes, peroxidase, myoglobin, and hemoglobin that are widely distributed in human body. Thus, hemin is a biocompatible molecule and suitable candidate as a stabilizer for few-layer Bi_2Se_3. It also contains a tetrapyrrole macrocycle, and the macrocycle is essentially planar structure, which trends to adsorb on the surface of 2D nanomaterials through π-π stack, hydrophobic and van der Waals interactions[55]. Therefore, hemin benefits the exfoliation of bulk Bi_2Se_3 and stabilization of few-layer Bi_2Se_3. Second, the macrocycle of hemin also benefits the adsorption of $A\beta_{1-42}$ monomer through π-π stack, hydrophobic and van der Waals interactions because one $A\beta_{1-42}$ monomer contains four aromatic amino acids (three phenylalanines and one tyrosine) and three heterocyclic amino acids (three histidines) (Supplementary Fig. S20). Third, it has been reported that hemin inhibits Aβ aggregation[56]. Our experimental data in Fig. 3e also confirmed the result even though the inhibition efficiency was lower than that of few-layer Bi_2Se_3. Therefore, the synergistic effect of hemin and few-layer Bi_2Se_3 might enhance the inhibition efficiency. The UV-vis spectra, XRD, SEM, TEM and AFM images of few-layer Bi_2Se_3 indicated that few-layer Bi_2Se_3 had been successfully prepared. XPS and TGA data show that 11.8% hemin was adsorbed on the surface of few-layer Bi_2Se_3. Furthermore, we used fractional centrifugation to obtain few-layer Bi_2Se_3 with different sizes and thicknesses, which was confirmed by UV-Vis spectrum, SEM, TEM and AFM images.

Few-layer Bi_2Se_3 with different thicknesses were used to evaluate their effect on inhibiting $A\beta_{1-42}$ fibril formation. ThT fluorescence assay was used to probe inhibition efficiency due to its strong fluorescence emission upon binding to cross-β fibrils[47-49]. The inhibition efficiency increased with increasing concentration of few-layer Bi_2Se_3. All few-layer Bi_2Se_3 with different layers had higher inhibition efficiency than that of hemin, and the inhibition efficiency increased with decreasing layer of few-layer Bi_2Se_3, which could be attributed to the adsorption of Aβ monomer on the surface of few-layer Bi_2Se_3. The thin few-layer Bi_2Se_3 had a larger specific area than that of thick few-layer Bi_2Se_3 because specific area increases with decreasing layer of few-layer Bi_2Se_3, which benefits adsorption of $A\beta_{1-42}$ monomer. We propose that after adsorption on few-layer Bi_2Se_3, the concentration of free $A\beta_{1-42}$ monomer in solution is low and therefore there is a reduction in fibril formation. $A\beta_{1-42}$ monomers, oligomers and fibrils have different morphologies, sizes, molecular weight and conductivities. According to their different morphologies, TEM and AFM images (Fig. 4) support the result that few-layer Bi_2Se_3 inhibits $A\beta_{1-42}$ fibril formation. According to their different sizes, DLS has showed that few-layer Bi_2Se_3 inhibits $A\beta_{1-42}$ fibril formation (Fig. 5). According to their different molecular weights and conductivities, PAGE and CVs also confirm the inhibition effect of few-layer Bi_2Se_3 on $A\beta_{1-42}$ fibril formation.

To understand the inhibition mechanism due to the adsorption of $A\beta_{1-42}$ monomer on few-layer Bi_2Se_3, we performed CD, CVs, electrochemical impedance, microbalance, XPS and EDX experiments. CD spectra showed that few-layer Bi_2Se_3 prevented the β-sheet structure formation. To further understand this mechanism, CVs, Nyquist diagrams, XPS, EDX mapping before and after adsorption of $A\beta_{1-42}$ monomers were collected. The decreasing conductivity and increasing contents of carbon, nitrogen and oxygen support the result that $A\beta_{1-42}$ monomer was adsorbed onto the surface of few-layer Bi_2Se_3. EDX mappings also supported the result that $A\beta_{1-42}$ monomer was uniformly distributed on the surface of few-layer Bi_2Se_3. The dynamic adsorptive process was further examined by investigating the impedance change and weight increment with time. Adsorption reached equilibrium at 20 min, and the dynamic adsorptive process was well-described by a pseudo-first-order kinetic model.

Furthermore, few-layer Bi_2Se_3 reduced Aβ-mediated peroxidase-like activity and the resulting complex of $A\beta_{1-42}$ and few-layer Bi_2Se_3 reduced glial C6 cells toxicities in comparison to those treated with mature $A\beta_{1-42}$ fibrils formed in the absence of few-layer Bi_2Se_3. The results suggest that the negatively charged few-layer Bi_2Se_3 in the microgram range could potentially serve as an Aβ inhibitor to prevent cell death caused by those detrimental Aβ species.

In summary, we have prepared a new Aβ inhibitor by a simple process. The most important discovery is that few-layer Bi_2Se_3 might serve as an Aβ inhibitor and exhibit higher inhibition efficiency against $A\beta_{1-42}$ fibril formation than hemin. The high inhibition efficiency of few-layer Bi_2Se_3 may be attributed to its high adsorption capacity for $A\beta_{1-42}$ monomer. Furthermore, few-layer Bi_2Se_3, with a good biocompatibility, may reduce enhanced peroxidase-like activity and the cytoxicity induced by $A\beta_{1-42}$. We can envision that few-layer Bi_2Se_3 may have the potential for applications in the biomedical field. The metabolism of few-layer Bi_2Se_3 *in vivo* and its possible biomedical applications will be investigated in our future work.

Methods

Synthesis of bulk Bi_2Se_3. Bulk Bi_2Se_3 was synthesized as we previously reported[44]. Polyvinyl pyrrolidone (0.9 g) was dissolved in 36 mL of ethylene glycol (EG). Then bismuth oxide powder (1 mmol), selenium powder (3 mmol) and ethylenediamine tetraacetic acid powder (4 mmol) were added into above-mentioned EG. The resulting suspension was stirred vigorously and subsequently sealed in a steel autoclave. The autoclave was heated to 200°C in 30 min and maintained over 20 h for a completed reaction. The as-obtained product was collected by centrifugation at 8000 rpm for 15 min, then washed three times with deionized water and absolute ethanol, and finally dried at 60°C for 96 h in an oven.

Preparation of few-layer Bi_2Se_3. Stock solution of hemin (0.05 mg mL^{-1}) was prepared in 0.1% $NH_3{\cdot}H_2O$ aqueous solution. The prepared bulk Bi_2Se_3 (100 mg) was dispersed in 200 mL of hemin solution by sonication for 40 h in a sonic bath (KQ-250 DB, 250 W). The resulting dispersion was left to stand for 48 h to allow any unstable aggregates to form. The supernatant was centrifuged at 2000 rpm for 20 min. The precipitate was collected as sample 2000 rpm. After centrifugation, the supernatant was collected and centrifuged at 6000 rpm for 20 min, and the precipitate was collected as sample 6000 rpm. Then, the remaining supernatant was centrifuged at 10000 rpm for 20 min, and the precipitate was collected as sample 10000 rpm. Finally, the collected supernatant was further centrifuged at 13000 rpm for 20 min, and the precipitate was collected as sample 13000 rpm.

Characterization of bulk Bi_2Se_3 and few-layer Bi_2Se_3. The micrographs of as-obtained bulk Bi_2Se_3 and few-layer Bi_2Se_3 were taken using JEOL JEM-2100 TEM (Tokyo, Japan) with an accelerating voltage of 200 kV and LEO-1530 field-emission SEM with an accelerating voltage of 20 kV. The samples were prepared by placing 20 μL of the colloidal solutions on copper grids coating with lacey carbon film for TEM or on small pieces of silicon wafer (P-100) for SEM, and were allowed to dry in air. AFM images were acquired in tapping mode in air using a Digital Instrument Nanoscope®. The samples were prepared by placing 20 μL of 10-fold diluted solutions onto the freshly cleaved mica for 5 min, gently rinsed with deionized water, and dried in vacuum overnight. XRD (Philips PANalytical X'Pert) equipped with Cu Ka radiation ($\lambda = 1.542$ Å) over the 2θ range of 10–80° was used to characterize the structure of few-layer Bi_2Se_3. Sample was prepared by depositing a film on the surface of glass slid. The UV–vis absorption spectra were measured on UV–vis spectrometer (UV-2550, Shimadzu), equipped with 1 cm quartz cells. The spectra were recorded in the wavelength range of 200–800 nm at a scan speed of 400 nm min^{-1}.

Preparation of Aβ monomer solution. The $A\beta_{1-42}$ monomer stock solution (200 μM) was prepared according to the previous reports[8]. Briefly, 1 mg lyophilized $A\beta_{1-42}$ (purity: 98.3%, measured by HPLC; molecule weight: 4514 Da, measured by mass spectrometry) synthesized by GL Biochem Ltd. (Shanghai, China) was dissolved in freshly prepared 942 μL of NaOH (10 mM) solution by sonication for 5 min under 100 W at ice cold condition. The peptide was fully dissolved under alkaline condition and existed only as monomer[57]. Peptide stock was stable in this form for 24 h at 4°C.

Effect of few-layer Bi_2Se_3 on $A\beta_{1-42}$ fibril formation. The previously prepared $A\beta_{1-42}$ monomer solution was mixed with designed volumes of few-layer Bi_2Se_3 (6 μg mL^{-1}) solution and then diluted by sterilized modified Krebs-Henseliet buffer to the final solution of 10 μM $A\beta_{1-42}$ with 0, 12, 60, 300 and 1200 ng mL^{-1} few-layer Bi_2Se_3, respectively. The samples were incubated at 37°C in 1.5 mL of Eppendorf tubes from 0 to 3 hours, and some of samples were taken out at the desired incubation time and used for the following measurements of ThT fluorescence, TEM, AFM, DLS, SDS-PAGE, CD, CVs, Nyquist diagrams and MTT assay. The physiologically-significant medium was a modified Krebs-Henseliet buffer including 118.5 mM sodium chloride, 4.8 mM potassium chloride, 1.2 mM magnesium sulfate, 1.4 mM calcium chloride, 11.0 mM glucose and it was buffered at pH 7.40 ± 0.05 with 100 mM Piperazine-1,4-bis(2-ethanesulfonic acid)[58]. The buffer also included 0.05% w/v sodium azide as an antimicrobial. All treatments were prepared and maintained at 37°C to accurately reflect physiological milieu.

ThT fluorescence assay. The fibril formation of $A\beta_{1-42}$ with or without inhibitors was evaluated by ThT fluorescence with a fluorescence spectrophotometer (FLS-920, Edinburgh Instruments). 50 μL of $A\beta_{1-42}$ (200 μM) was mixed with few-layer Bi_2Se_3 with different layers of required concentration and incubated in a 1.5 mL of sterile brown centrifuge tube, which included 10 μM ThT and 0.05% sodium azide in the modified Krebs-Henseliet buffer. The final volume was 1 mL. The Aβ concentration was fixed at 10 μM (45.14 μg mL^{-1}) and concentration of few-layer Bi_2Se_3 was changed from 0 to 1200 ng mL^{-1}. The samples were loaded on a thermomixer (Eppendorf, Germany) at 37°C for 0–3 h during which samples were collected and measured. Three replicates were performed and averaged.

TEM and AFM measurements. Final solution of 10 μM $A\beta_{1-42}$ with 0, 12, 60, 300 and 1200 ng mL^{-1} few-layer Bi_2Se_3 incubated at 37°C for 3 h were used for TEM and AFM measurements. The morphologies of $A\beta_{1-42}$ with and without few-layer Bi_2Se_3 were confirmed by TEM and AFM. For TEM measurements, samples were deposited on 400-mesh Formvar carbon-coated copper grids for 5 min. Negative staining was performed by using 2% uranyl acetate for 5 min and the grids were rinsed once with double

distilled water. The samples were examined with a JEOL JEM-2100 TEM with an accelerating voltage of 200 kV. For AFM measurements, 10 μL of samples were freshly prepared and swiftly diluted 10-fold in deionized water. 10 μL of the diluted sample was mounted onto the freshly cleaved mica for 5 min, gently rinsed with deionized water, and dried in vacuum overnight. Images were acquired under atmosphere in a tapping mode.

DLS. Samples of 20 μM $A\beta_{1-42}$ monomer, 20 μM $A\beta_{1-42}$ incubated at 37°C for 3 h with 0, 24 and 2400 ng mL^{-1} few-layer Bi_2Se_3, and 6 μg mL^{-1} few-layer Bi_2Se_3 were used for DLS measurements. The samples were 2-fold diluted in double distilled water and subjected to size analysis by Zetasizer Nano (Malvern Instruments, Worchestershire, UK) using disposable solvent resistant micro cuvette (ZEN0040) at room temperature.

SDS-PAGE and Native-PAGE analysis. 20 μM $A\beta_{1-42}$ monomer, 20 μM $A\beta_{1-42}$ incubated at 3 h with 0, 24, 120, 600 and 2400 ng mL^{-1} few-layer Bi_2Se_3 were used for SDS or Native-PAGE analysis. For SDS-PAGE analysis, the samples (10 μL) were mixed with 2× PAGE sample loading buffer (10 μL). Then samples were run on 12% PAGE gel at 80 V for 0.5 h followed by 120 V for 1.5 h. The gel was stained by coomassie blue. For Native-PAGE analysis, samples were run on 12% Tris/glycine gel at 100 V for 10 min followed by 200 V for 0.5 h. The gel was stained using silver stain and the relative quantity was estimated using Bio-Rad's Image Lab 4.1 software. The bands were both visualized using gel imaging and analysis system (Bio-rad Gel Doc XR).

CD spectra. 20 μM $A\beta_{1-42}$ monomer, 20 μM $A\beta_{1-42}$ incubated at 3 h with and without 0, 120, and 2400 ng mL^{-1} few-layer Bi_2Se_3 were used for CD spectra. The CD spectra were measured from 190 to 260 nm at room temperature on a Jasco J-810 spectrometer (Tokyo, Japan) using a cell with a path length of 0.1 cm. Data were collected every 0.2 nm with 3 nm bandwidth at a scan speed of 50 nm min^{-1} and response time of 4 seconds. All spectra were collected in a triplicate and a background-corrected against buffer blank.

Inhibiting $A\beta_{1-42}$ fibril formation by CVs. 10 μM of $A\beta_{1-42}$ monomer, 10 μM $A\beta_{1-42}$ incubated at 37°C for 3 h with 0, and 1200 ng mL^{-1} few-layer Bi_2Se_3, and 1200 ng mL^{-1} few-layer Bi_2Se_3 were used for CVs measurements. The glass-carbon electrode (GCE, $\Phi = 3$ mm) was polished with 0.3 and 0.05 μm alumina slurry, rinsed thoroughly with doubly distilled water between each polishing step, then GCE was washed successively with 1:1 nitric acid, ethanol, and doubly distilled water in an ultrasonic bath and dried in air. 10 μL of samples were dropped onto the GCE to prepare modified electrodes. CVs measurements were performed on an electrochemical workstation (CHI660C, CH Instrument, USA). The three-electrode system consisted of a platinum wire as auxiliary electrode and an Ag/AgCl (saturated KCl) as reference. Working electrodes were GCEs modified with samples. CV measurements were performed in 6.0 mM $K_3[Fe(CN)_6]$ and 1.0 M KCl solution with the scan rate of 100 mV s^{-1}.

Adsorption by CVs and impedance measurements. 10 μL of few-layer Bi_2Se_3 (10 μg mL^{-1}) was dropped onto the GCE to prepare few-layer Bi_2Se_3-modified electrode. For adsorbing $A\beta_{1-42}$ monomer, few-layer Bi_2Se_3-modified electrode was immersed in modified Krebs-Henseliet buffer containing 10 μM $A\beta_{1-42}$ monomer for 10 min, and then immersed in modified Krebs-Henseliet buffer for 30 seconds to remove free $A\beta_{1-42}$ monomers. Few-layer Bi_2Se_3-modified electrode before and after adsorbing $A\beta_{1-42}$ monomer were used for CVs and impedance measurements. CVs were performed almost the same as above. The impedance measurements were performed in 5.0 mM $[Fe(CN)_6]^{3-/4-}$ and 1.0 M KCl solution. The AC voltage amplitude was 5 mV and the voltage frequencies ranged from 0.1 Hz to 10^5 Hz.

Adsorption kinetics process by impedance measurements and real-time weight measurements. The impedance measurement with time was performed in modified Krebs-Henseliet buffer at 10 Hz. Few-layer Bi_2Se_3-modified electrode was subjected to successive incubations first in modified Krebs-Henseliet buffer without $A\beta_{1-42}$ as a pre-equilibration step. Buffer was added twice at 30 min and 90 min, respectively. $A\beta_{1-42}$ monomer was added at 60 min.

Real-time weight measurement was performed on a microbalance (KSV NIMA). Silicon wafer was washed successively with 1:1 nitric acid, ethanol, and doubly distilled water in an ultrasonic bath and dried in air. 50 μL of few-layer Bi_2Se_3 (10 μg mL^{-1}) dispersion was dropped onto silicon wafer to prepare few-layer Bi_2Se_3-coated silicon wafer. Then the modified silicon wafer was dried naturally overnight. Then few-layer Bi_2Se_3-coated silicon wafer was hung on a microbalance and immersed in modified Krebs-Henseliet buffer containing 10 μM $A\beta_{1-42}$ monomers. Thus, the weight of adsorbed $A\beta_{1-42}$ monomers was *in situ* monitored.

Inhibition of Aβ-mediated peroxidase-like activity. The inhibition assay of Aβ-mediated peroxidase-like activity was performed as follows. Firstly, 12 μg mL^{-1} of few-layer Bi_2Se_3 or 1.416 μg mL^{-1} of hemin in the presence and absence of 50 μM $A\beta_{1-42}$ monomers were incubated at 37°C for 0 h or 3 h in a 1.5 mL of sterile centrifuge tube and served as catalyst for peroxidase-like activity assay. Kinetic measurements were carried out in time course mode by monitoring the absorbance change at 652 nm on a TU-1901 UV-vis spectrophotometer. Peroxidase-like activity experiments were performed using the

above samples as catalyst in a reaction volume of 600 μL acetic acid-sodium acetate buffer solution (0.02 M, pH 4, 25°C) with 100 μM 3,3′,5,5′-Tetramethylbenzidine as substrate and 10 mM hydrogen peroxide.

Inhibition of Aβ-mediated cytotoxicity. The rabbit glial C6 cells (from cell storeroom of Chinese Academy of Sciences) were incubated at 37°C under 5% CO_2, and were cultured in DMEM media (Gibco, Invitrogen, Carlsbad, CA, USA) with 10% fetal bovine serum (FBS) (Biological Industry, Kibbutz Beit-Haemek, Israel) in a humid camber. A total of 1×10^5 cells were seeded overnight in the growth medium in a polystyrene 96-well plate (Corning, NY, USA). The growth medium was then discarded and the cells were washed twice by 1×phosphate buffered saline (PBS). 1×PBS was prepared by dissolving 0.24 g KH_2PO_4, 1.44 g Na_2HPO_4, 0.2 g KCl and 8.0 g NaCl into 1 L of water. pH was adjusted to 7.4 with HCl. The final concentration was 10 mM phosphate, 137 mM NaCl and 2.7 mM KCl. Then, the FBS-free media (50 μL) was added into each well. Next, the cells were treated with 50 μL of the end-point products as described in text. The cells were incubated for additional 24 h in the growth chamber and then 50 μL of MTT (5 mg mL^{-1} in DMEM without FBS) was added into each well and incubated for another 4 h. The media was discarded and dimethylsulfoxide was used to lyze the cells until the purple crystals were fully dissolved. Absorbance at 570 nm was measured by a microplate reader (SpectraMax M5, Molecule Devices). Three replicates were performed and the data were averaged (n = 3). Background signals from sample treatment without cells were subtracted. Each data set was normalized using the reading obtained from the buffer controls and the cytotoxicity data were obtained by subtracting the viability data from 100%.

References

1. Alzheimer's Association. 2012 Alzheimer's disease facts and figures. *Alzheimers Dement* **8,** 131–168 (2012).
2. Hardy, J. & Selkoe, D. J. The amyloid hypothesis of Alzheimer's disease: progress and problems on the road to therapeutics. *Science* **297,** 353–356 (2002).
3. Kang, J. *et al.* The precursor of Alzheimer's disease amyloid A4 protein resembles a cell-surface receptor. *Nature* **325,** 733–736 (1987).
4. Thinakaran, G. & Koo, E. H. Amyloid precursor protein trafficking, processing, and function. *J. Biol. Chem.* **283,** 29615–29619 (2008).
5. Pollock, V. V., Pastoor, T. E. & Wecker, L. Cyclic AMP-dependent protein kinase (PKA) phosphorylates Ser362 and 467 and protein kinase C phosphorylates Ser550 within the M3/M4 cytoplasmic domain of human nicotinic receptor alpha4 subunits. *J. Neurochem.* **103,** 456–466 (2007).
6. Schoonenboom, N. S. *et al.* Amyloid beta 38, 40, and 42 species in cerebrospinal fluid: more of the same? *Ann. Neurol.* **58,** 139–142 (2005).
7. Hellstrand, E., Boland, B., Walsh, D. M. & Linse, S. Amyloid beta-protein aggregation produces highly reproducible kinetic data and occurs by a two-phase process. *ACS Chem. Neurosci.* **1,** 13–18 (2010).
8. Mold, M., Ouro-Gnao, L., Wieckowski, B. M. & Exley, C. Copper prevents amyloid-beta(1-42) from forming amyloid fibrils under near-physiological conditions *in vitro*. *Sci. Rep.* **3,** 1256 (2013).
9. Liao, Y. H., Chang, Y. J., Yoshiike, Y., Chang, Y. C. & Chen, Y. R. Negatively charged gold nanoparticles inhibit Alzheimer's amyloid-beta fibrillization, induce fibril dissociation, and mitigate neurotoxicity. *Small* **8,** 3631–3639 (2012).
10. Li, M. *et al. In situ* monitoring Alzheimer's disease beta-amyloid aggregation and screening of Abeta inhibitors using a perylene probe. *Small* **9,** 52–55 (2013).
11. Lanz, T. A. *et al.* Concentration-dependent modulation of amyloid-beta *in vivo* and *in vitro* using the gamma-secretase inhibitor, LY-450139. *J. Pharmacol. Exp. Ther.* **319,** 924–933 (2006).
12. Lee, H. G. *et al.* Amyloid-beta in Alzheimer disease: the null versus the alternate hypotheses. *J. Pharmacol. Exp. Ther.* **321,** 823–829 (2007).
13. Re, F. *et al.* Beta amyloid aggregation inhibitors: small molecules as candidate drugs for therapy of Alzheimer's disease. *Curr. Med. Chem.* **17,** 2990–3006 (2010).
14. Hamaguchi, T., Ono, K. & Yamada, M. Anti-amyloidogenic therapies: strategies for prevention and treatment of Alzheimer's disease. *Cell. Mol. Life Sci.* **63,** 1538–1552 (2006).
15. LeVine, H., 3rd. Small molecule inhibitors of Abeta assembly. *Amyloid* **14,** 185–197 (2007).
16. Nie, Q., Du, X. G. & Geng, M. Y. Small molecule inhibitors of amyloid beta peptide aggregation as a potential therapeutic strategy for Alzheimer's disease. *Acta Pharmacol. Sin.* **32,** 545–551 (2011).
17. Cheng, A. C. *et al.* Structure-based maximal affinity model predicts small-molecule druggability. *Nat. Biotechnol.* **25,** 71–75 (2007).
18. Wells, J. A. & McClendon, C. L. Reaching for high-hanging fruit in drug discovery at protein-protein interfaces. *Nature* **450,** 1001–1009 (2007).
19. Gestwicki, J. E., Crabtree, G. R. & Graef, I. A. Harnessing chaperones to generate small-molecule inhibitors of amyloid beta aggregation. *Science* **306,** 865–869 (2004).
20. Shaw, C. P., Middleton, D. A., Volk, M. & Lévy, R. Amyloid-derived peptide forms self-assembled monolayers on gold nanoparticle with a curvature-dependent β-sheet structure. *ACS nano* **6,** 1416–1426 (2012).
21. Mahmoudi, M. *et al.* Influence of the physiochemical properties of superparamagnetic iron oxide nanoparticles on amyloid β protein fibrillation in solution. *ACS Chem. Neurosci.* **4,** 475–485 (2013).
22. Yoo, S. I. *et al.* Inhibition of amyloid peptide fibrillation by inorganic nanoparticles: functional similarities with proteins. *Angew. Chem Int. Ed.* **50,** 5110–5115 (2011).
23. Siemers, E. *et al.* Safety, tolerability, and changes in amyloid beta concentrations after administration of a gamma-secretase inhibitor in volunteers. *Clin. Neuropharmacol.* **28,** 126–132 (2005).
24. Mahmoudi, M., Akhavan, O., Ghavami, M., Rezaee, F. & Ghiasi, S. M. Graphene oxide strongly inhibits amyloid beta fibrillation. *Nanoscale* **4,** 7322–7325 (2012).
25. Li, H., Luo, Y., Derreumaux, P. & Wei, G. Carbon nanotube inhibits the formation of β-sheet-rich oligomers of the Alzheimer's amyloid-β(16-22) peptide. *Biophys. J.* **101,** 2267–2276 (2011).
26. Gao, N. *et al.* Transition-metal-substituted polyoxometalate derivatives as functional anti-amyloid agents for Alzheimer's disease. *Nat. Commun.* **5,** 3422 (2014).

27. Pedersen, J. T. *et al.* Rapid exchange of metal between Zn7-metallothionein-3 and amyloid-β peptide promotes amyloid-related structural changes. *Biochemistry* **51,** 1697–1706 (2012).
28. Pramanik, D., Ghosh, C. & Dey, S. G. Heme–Cu bound Aβ peptides: spectroscopic characterization, reactivity, and relevance to Alzheimer's Disease. *J. Am. Chem. Soc.* **133,** 15545–15552 (2011).
29. Chen, Y. *et al.* Experimental realization of a three-dimensional topological insulator, Bi_2Te_3. *Science* **325,** 178–181 (2009).
30. Hsieh, D. *et al.* A topological Dirac insulator in a quantum spin Hall phase. *Nature* **452,** 970–974 (2008).
31. Moore, J. Topological insulators: the next generation. *Nat. Phys.* **5,** 378–380 (2009).
32. Xia, Y. *et al.* Observation of a large-gap topological-insulator class with a single Dirac cone on the surface. *Nat. Phys.* **5,** 398–402 (2009).
33. Kong, D. & Cui, Y. Opportunities in chemistry and materials science for topological insulators and their nanostructures. *Nat. Chem.* **3,** 845–849 (2011).
34. Shahil, K., Hossain, M., Goyal, V. & Balandin, A. Micro-Raman spectroscopy of mechanically exfoliated few-quintuple layers of Bi_2Te_3, Bi_2Se_3, and Sb_2Te_3 materials. *J. Appl. Phys.* **111,** 054305 (2012).
35. Hernandez, Y. *et al.* High-yield production of graphene by liquid-phase exfoliation of graphite. *Nat. Nanotechnol.* **3,** 563–568 (2008).
36. Coleman, J. N. *et al.* Two-dimensional nanosheets produced by liquid exfoliation of layered materials. *Science* **331,** 568–571 (2011).
37. Nicolosi, V., Chhowalla, M., Kanatzidis, M. G., Strano, M. S. & Coleman, J. N. Liquid exfoliation of layered materials. *Science* **340,** 1226419 (2013).
38. Wu, S., Liu, G., Li, P., Liu, H. & Xu, H. A high-sensitive and fast-fabricated glucose biosensor based on prussian blue/topological insulator Bi_2Se_3 hybrid film. *Biosens Bioelectron* **38,** 289–294 (2012).
39. Chen, S. *et al.* Study on the electrochemical catalytic properties of the topological insulator Bi_2Se_3. *Biosens Bioelectron* **46,** 171–174 (2013).
40. Li, J. *et al.* Topological insulator bismuth selenide as a theranostic platform for simultaneous cancer imaging and therapy. *Sci. Rep.* **3,** 1998–2005 (2013).
41. Zhang, X. D. *et al.* Metabolizable Bi_2Se_3 nanoplates: biodistribution, toxicity, and uses for cancer radiation therapy and imaging. *Adv. Funct. Mater.* **24,** 1718–1729 (2013).
42. Kong, L. *et al.* The suppression of prostate LNCaP cancer cells growth by Selenium nanoparticles through Akt/Mdm2/AR controlled apoptosis. *Biomaterials* **32,** 6515–6522 (2011).
43. Xue, T. *et al.* Graphene-supported hemin as a highly active biomimetic oxidation catalyst. *Angew. Chem.* **124,** 3888–3891 (2012).
44. Sun, L. P. *et al.* Preparation of few-Layer bismuth selenide by liquid-phase-exfoliation and its optical absorption properties. *Sci. Rep.* **4,** 4794–4802 (2014).
45. Sun, Y., *et al.* Atomically thick bismuth selenide freestanding single layers achieving enhanced thermoelectric energy harvesting. *J. Am. Chem. Soc.* **134,** 20294–20297 (2012).
46. Zhang, J. *et al.* Raman spectroscopy of few-quintuple layer topological insulator Bi_2Se_3 nanoplatelets. *Nano Lett.* **11,** 2407–2414 (2011).
47. LeVine, H., III. Quantification of β-sheet amyloid fibril structures with thioflavin T. *Methods Enzymol.* **309,** 274–284 (1999).
48. Biancalana, M. & Koide, S. Molecular mechanism of Thioflavin-T binding to amyloid fibrils. *Biochim. Biophys. Acta* **1804,** 1405–1412 (2010).
49. Nilsson, M. R. Techniques to study amyloid fibril formation *in vitro*. *Methods* **34,** 151–160 (2004).
50. Manavalan, P. & Johnson, W. C. Sensitivity of circular dichroism to protein tertiary structure class. *Nature* **305,** 831–832 (1983).
51. Kumar, K. V. Linear and non-linear regression analysis for the sorption kinetics of methylene blue onto activated carbon. *J. Hazard. Mater.* **137,** 1538–1544 (2006).
52. Outeiro, T. F. Amyloidogenesis: FlAsH illuminates Abeta aggregation. *Nat. Chem. Biol.* **7,** 581–582 (2011).
53. Kumar, S. *et al.* Extracellular phosphorylation of the amyloid beta-peptide promotes formation of toxic aggregates during the pathogenesis of Alzheimer's disease. *EMBO J.* **30,** 2255–2265 (2011).
54. Cassagnes, L. E. *et al.* The catalytically active copper-amyloid-beta state: coordination site responsible for reactive oxygen species production. *Angew. Chem.* **125,** 11316–11319 (2013).
55. Lv, X. & Weng, J. Ternary composite of hemin, gold nanoparticles and graphene for highly efficient decomposition of hydrogen peroxide. *Sci. Rep.* **3,** 3285 (2013).
56. Howlett, D., Cutler, P., Heales, S. & Camilleri, P. Hemin and related porphyrins inhibit β-amyloid aggregation. *FEBS Lett.* **417,** 249–251 (1997).
57. Choi, H. D., Seo, P. J., Son, B. W. & Kang, B. W. Synthesis of 5-chloro-3-[4-(3-diethylaminopropoxy)benzoyl]-2-(4-methoxyphenyl) benzofuran as a beta-amyloid aggregation inhibitor. *Arch. Pharm. Res.* **26,** 985–989 (2003).
58. Higashi, S. & Miyazaki, K. Novel processing of beta-amyloid precursor protein catalyzed by membrane type 1 matrix metalloproteinase releases a fragment lacking the inhibitor domain against gelatinase A. *Biochemistry* **42,** 6514–6526 (2003).

Acknowledgements

This work is supported by the National Key Scientific Research Projects (2014CB932004), National Natural Science Foundation of China (31371005 and 81171453), the Knowledge Innovation Program of Shenzhen City (JCYJ20130327150937484), the Fundamental Research Funds for the Central Universities and Program for New Century Excellent Talents in University, the Ministry of Education.

Author Contributions

J.W. and L.P.S. conceived the work. J.P. and Z.Q.L. performed the preparation and characterization of materials. J.P. and Y.J.X. performed the application of the materials. All authors analysed the data and prepared the manuscript.

Additional Information

Supplementary information accompanies this paper at http://www.nature.com/srep

Competing financial interests: The authors declare no competing financial interests.

How to cite this article: Peng, J. *et al.* Few-layer bismuth selenides exfoliated by hemin inhibit amyloid-ß$_{1-42}$ fibril formation. *Sci. Rep.* **5**, 10171; doi: 10.1038/srep10171 (2015).